

OPEN ACCESS

## Lactone-Based Liquid Electrolytes for Fluoride Shuttle Batteries

To cite this article: Mitsuo Kawasaki *et al* 2021 *J. Electrochem. Soc.* **168** 010529

View the [article online](#) for updates and enhancements.



### ECS Membership = Connection

**ECS membership connects you to the electrochemical community:**

- Facilitate your research and discovery through ECS meetings which convene scientists from around the world;
- Access professional support through your lifetime career;
- Open up mentorship opportunities across the stages of your career;
- Build relationships that nurture partnership, teamwork—and success!


**Join ECS!**

**Visit [electrochem.org/join](https://electrochem.org/join)**





# Lactone-Based Liquid Electrolytes for Fluoride Shuttle Batteries

Mitsuo Kawasaki,<sup>1,z</sup>  Ken-Ichi Morigaki,<sup>1</sup> Gentaro Kano,<sup>1</sup> Hirofumi Nakamoto,<sup>1</sup> Reiji Takekawa,<sup>2</sup> Junichi Kawamura,<sup>2</sup> Taketoshi Minato,<sup>3</sup> Takeshi Abe,<sup>4,\*</sup> and Zempachi Ogumi<sup>1,\*\*</sup>

<sup>1</sup>Office of Society-Academia Collaboration for Innovation, Kyoto University, Gokasho, Uji, Kyoto 611-0011, Japan

<sup>2</sup>Institute of Multidisciplinary Research for Advanced Materials, Tohoku University, Aoba-ku, Sendai, 980-8577, Japan

<sup>3</sup>Office of Society-Academia Collaboration for Innovation, Kyoto University, Katsura, Nishikyo, Kyoto 615-8530, Japan

<sup>4</sup>Graduate School of Global Environmental Studies, Kyoto University, Katsura, Nishikyo, Kyoto 615-8510, Japan

Rechargeable secondary batteries operating through fluoride-ion shuttling between the positive and negative electrodes, referred to as fluoride shuttle batteries (FSBs), offer a potentially promising solution to overcoming the energy-density limitations of current lithium-ion battery systems. However, there are many technical issues that need to be resolved to achieve high-quality fluoride-carrying electrolytes and ensure reversible transformations between a metal and its fluoride counterpart at both electrodes. Here, we introduce novel lactone-based liquid electrolytes consisting either of CsF or KF, which are prepared by a solvent substitution method. Although the maximum fluoride-ion concentration achieved by the method is approximately 0.05 M, these systems behave as strong electrolytes where CsF(KF) is almost fully dissociated into Cs<sup>+</sup>(K<sup>+</sup>) and F<sup>-</sup> ions to give a maximum ionic conductivity of 0.8 mS.cm<sup>-1</sup>. Hence, the solvent supports electrochemically active fluoride ions that can drive reversible metal/metal-fluoride transformations at room temperature for a wide range of metal electrodes. However, irreversible reductive reactions of the solvent, also promoted by the fluoride ions, limit currently the negative potential window to approximately -1.5 V vs the standard hydrogen electrode.

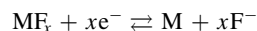
© 2021 The Author(s). Published on behalf of The Electrochemical Society by IOP Publishing Limited. This is an open access article distributed under the terms of the Creative Commons Attribution Non-Commercial No Derivatives 4.0 License (CC BY-NC-ND, <http://creativecommons.org/licenses/by-nc-nd/4.0/>), which permits non-commercial reuse, distribution, and reproduction in any medium, provided the original work is not changed in any way and is properly cited. For permission for commercial reuse, please email: [permissions@iopublishing.org](mailto:permissions@iopublishing.org). [DOI: [10.1149/1945-7111/abdafj](https://doi.org/10.1149/1945-7111/abdafj)]



Manuscript submitted October 7, 2020; revised manuscript received December 20, 2020. Published January 21, 2021.

Supplementary material for this article is available [online](#)

Fluoride shuttle batteries (FSBs) are rechargeable batteries based on the transport of fluoride ions as charge carriers and redox-active species.<sup>1,2</sup> These systems offer a high electrochemical energy storage capability that could potentially exceed those of the state-of-the-art lithium-ion batteries (LIBs).<sup>3-5</sup> This potential can be attributed to the unique properties of the monovalent fluoride ion. It is the lightest halide, difficult to oxidize, and yet capable of reacting with various metals to form mono- and multi-valent fluoride species with large formation energies. This behavior leads to anion-based redox reactions of single- or multi-electron transfer, according to the following reversible half-cell reactions.



The theoretical gravitational capacities for some typical metal (M)/metal-fluoride (MF<sub>x</sub>) combinations, defined by  $xF/3.6/W_M$  ( $F$  the Faraday constant and  $W_M$  the atomic weight of the respective metal), are 249, 844, 385, and 2980 mAh/g-metal for Ag/AgF, Cu/CuF<sub>2</sub>, Bi/BiF<sub>3</sub>, and Al/AlF<sub>3</sub>, respectively. These values also scale with remarkably large volumetric capacities of 2612, 7545, 3765, and 8046 mAh cm<sup>-3</sup>, respectively.

In a study by Reddy and Fichtner,<sup>1</sup> a solid electrolyte, La<sub>1-x</sub>Ba<sub>x</sub>F<sub>3-x</sub>, was used in combination with composites of various metal fluorides as positive electrodes and Ce metal as a negative electrode. They addressed various mechanistic issues and technical limitations associated with the all-solid-state cells, reporting that they could operate only at a high temperature of 150 °C. Mohammad and co-workers recently demonstrated the feasibility of a room temperature FSB,<sup>6</sup> based on BaSnF<sub>4</sub> as a solid electrolyte with a higher ionic conductivity than previously available. They found that a Zn|BaSnF<sub>4</sub>|BiF<sub>3</sub> cell had relatively stable cycling at room temperature, but the overall cell performance was still limited.

Liquid-electrolyte-based FSBs that are more suitable for room temperature operations have also drawn considerable interest and

much effort has been made to develop fluoride-ion-carrying electrolytes with high electrochemical stability. Normally, alkali fluorides are poorly soluble in organic solvents with high boiling points that are suitable for rechargeable batteries. One solution to this problem has been to use organic fluoride salts (such as alkylammonium or substituted alkylammonium fluorides). Using this type of fluoride salt in combination with an ionic liquid, Okazaki and co-workers reported on the operation of a rechargeable FSB with a Bi needle or tip as the positive electrode and a PbF<sub>2</sub> coated Pb plate as the negative electrode.<sup>7</sup> However, the cell performance deteriorated with a rapid capacity fading under cycling. Recently, Davis and co-workers reported that neopentyl-substituted alkylammonium fluorides in combination with ether solvents are superior fluoride-ion conducting liquid electrolytes for room-temperature FSB operation.<sup>8</sup> However, because of cathode-metal-dissolution problems, the reversible room-temperature operation has only been achieved for a Cu-LaF<sub>3</sub> core-shell electrode. This system has a limited capacity restricted by solid-state fluoride ion transport through the LaF<sub>3</sub> shell to/from the Cu core.

Another way to develop liquid-electrolyte FSBs is to use a so-called anion acceptor (AA) that makes the alkali fluorides more-or-less soluble even in low-polarity solvents such as the glyme series. Konishi and co-workers have proposed that AAs may play another important role in facilitating the dissolution and re-deposition of the active materials into/from the electrolyte.<sup>9-11</sup> This reaction pathway is unique to liquid-electrolyte-based FSBs and careful control may yield considerable gains in cell capacity and cyclability. However, the concentration of AAs at which they can play these dual roles may not necessarily be small enough to ensure overall electrolyte stability. Control over the solubility of the active material is likely to be difficult because even relatively minor dissolution of positive-electrode materials and diffusion toward the negative electrode might later interfere with the rechargeable operation of the FSB cell.

In this article, as a first step to developing fluoride-ion-transporting liquid electrolytes better suited for the construction of stable FSB cells, we introduce lactone ( $\gamma$ -butyrolactone, GBL)-based liquid electrolytes, denoted as CsF(KF)/GBL. In these systems, either CsF or KF fully dissociated aided only by solvation in GBL. We report a

\*Electrochemical Society Member.

\*\*Electrochemical Society Fellow.

<sup>z</sup>E-mail: [m-kawasaki@saci.kyoto-u.ac.jp](mailto:m-kawasaki@saci.kyoto-u.ac.jp)

novel fabrication method to achieve this state, which behaves as a strong electrolyte satisfying Kohlrausch's law.<sup>12,13</sup> Although the maximum fluoride ion concentration achieved by the method was approximately 0.05 M, the electrolyte gives an ionic conductivity as high as 0.8 mS cm<sup>-1</sup>. Furthermore, the fluoride ions exhibited high electrochemical activities for various metals undergoing reversible metal/metal-fluoride transformations.

An issue that remains to be addressed through further studies on practical applications of CsF(KF)/GBL is the fact that the presence of highly active free F<sup>-</sup> ions in the electrolyte promotes irreversible reductive decomposition of the solvent, restricting the negative potential window. However, this is also a unique behavior of novel non-aqueous fluoride electrolytes, which gives valuable insights for the future design of room-temperature FSBs.

## Experimental

**Materials.**—Solid powders of cesium fluoride (CsF) and potassium fluoride (KF) were purchased from Tokyo Chemical Industry.  $\gamma$ -Butyrolactone of lithium-ion battery grade and lithium bis (fluorosulfonyl)imide (LiFSA) were obtained from Kishida Chemical Co. Ltd. (Osaka, Japan). Ferrocene was from Sigma-Aldrich. Ultrapure water was prepared by a Direct-QUV3 water purification system (Merck KGaA, Darmstadt, Germany) for the preparation of the relevant aqueous solutions. High purity metals (in the form of plate, foil, mesh, or wire) were received from Nilaco Corporation (Tokyo, Japan). A nickel sponge was from Sumitomo Electric Industries, Ltd. (Osaka, Japan). All the other chemicals were of special reagent grade and used as received from Fujifilm Wako Pure Chemical Corporation (Osaka, Japan) or Kanto Chemical Co., Ltd. (Tokyo, Japan).

### Elemental analyses and ionic conductivity measurements.

The atomic concentration of the metal (cationic) species constituting the liquid electrolytes was measured by either atomic absorption spectroscopy (AAS) with a polarized Zeeman atomic absorption spectrophotometer (Hitachi, ZA3000) or inductively coupled plasma-mass spectrometry (Agilent 7700).

Nuclear magnetic resonance (NMR) measurements for the <sup>1</sup>H, <sup>13</sup>C, <sup>19</sup>F, and <sup>133</sup>Cs spectra were performed with a Bruker Avance III (11.7 T) NMR spectrometer. The resonance frequencies were 500.0, 125.7, 470.4, and 65.6 MHz for <sup>1</sup>H, <sup>13</sup>C, <sup>19</sup>F, and <sup>133</sup>Cs, respectively. The chemical shifts were determined by referencing the following external standard materials; TMS (0 ppm for <sup>1</sup>H and <sup>13</sup>C), fluorobenzene (-113.15 ppm for <sup>19</sup>F),<sup>14</sup> and 0.1 M aqueous CsNO<sub>3</sub> solution (0 ppm for <sup>133</sup>Cs), respectively.

The trace amount of water in the electrolytes was determined by the Karl Fischer titration method (Hiranuma, AQ-2200). The ionic conductivity was measured with a conductivity meter (Mettler Toledo, SG7).

**Electrochemical measurements.**—Electrochemical measurements, including cyclic voltammetry (CV) and chronopotentiometry (CP), were performed with an SP-240 potentiostat (BioLogic) using a three-electrode conical beaker cell (EC Frontier Co., Ltd. (Kyoto, Japan), VB7 cell kit). In the half-cell mode, the cell consisted of a working electrode made of the respective metal of interest (rectangular plate or foil), a counter electrode made of either platinum mesh or a porous nickel sponge or activated carbon composite, a silver wire reference electrode, and liquid electrolyte of 0.4 ml in total volume (cf. Fig. S1 is available online at [stacks.iop.org/JES/168/010529/mmedia](https://stacks.iop.org/JES/168/010529/mmedia)). The effective contact area of the metal electrode with the electrolyte, distinguishable by visible changes in the surface texture or color due to the electrochemical reactions, was typically 0.4 cm<sup>2</sup>. In the full-cell mode, the counter electrode was replaced by another metal electrode that had been pre-fluorinated in advance in the half-cell mode (see below for more detail). The whole cell-assembly during the measurements was placed either in a glove box filled with purified dry Ar gas (dew point < -83 °C) or in a low-pressure vacuum chamber

with a continuous dry Ar gas flow to maintain a steady-state Ar pressure of 10 kPa. The reference Ag electrode potential was calibrated with the use of ferrocene as an internal standard.<sup>15</sup>

**Structural characterization.**—The crystal structures of the active materials and their changes during the charge and discharge processes were examined by *ex-situ* X-ray diffraction (XRD) measurements with Cu K $\alpha$  radiation of 8.04 keV (Rigaku, SmartLab) with the use of an airtight specimen holder (Bruker, A100-B36) designed for environmentally sensitive materials. After the charging or discharging, the sample was removed from the electrolyte to an Ar-filled vacuum glove box, washed by GBL, dried under vacuum, mounted on the sample supporting table of the specimen holder, and tightly shielded from the air by a domed plastic cap. The changes in the surface morphologies and elemental distributions on the electrode surface by charging and discharge were inspected by a field emission scanning electron microscope (FE-SEM) and energy-dispersive X-ray spectroscopy (EDX) with Hitachi SU6600 and SU8200 instruments.

**Density functional theory (DFT) calculations.**—The optimum (minimum energy) structures of an F<sup>-</sup> ion coordinated by H<sub>2</sub>O or by GBL solvent molecules were calculated with the use of DFT. We applied calculation methods that have previously been used to estimate the molecular structures in electrolytes for rechargeable batteries.<sup>16–20</sup> Namely, BIOVIA Materials Studio D-mol3 with the B3LYP functional<sup>21,22</sup> was used in the calculations. The total (including all electrons) gas-phase binding energies of two or more interacting species relative to that of their isolated states in vacuum were calculated, according to the following relationship:

$$E_B = E(\text{F} - \text{Mol}) - [E(\text{F}^-) + E(\text{Mol})],$$

where  $E(\text{F-Mol})$ ,  $E(\text{F}^-)$ , and  $E(\text{Mol})$  are the total gas-phase energies for the F<sup>-</sup>-H<sub>2</sub>O or F<sup>-</sup>-GBL molecular complexes, an isolated F<sup>-</sup> ion, and an isolated H<sub>2</sub>O or GBL, respectively. Self-consistent field procedures led us to obtain well-converged geometrical and electronic structures at a convergence criterion of 10<sup>-6</sup> a.u.

## Results and Discussion

**Preparation and characterization of lactone-based liquid electrolyte.**—Of the two kinds of lactone (GBL) based electrolytes prepared by the present method, that consisting of CsF denoted as CsF/GBL gave the maximum fluoride concentration of ~0.05 M according to the AAS and ICP elemental analyses of Cs. A typical ionic conductivity of ~0.8 mS cm<sup>-1</sup> was measured. This is significantly large for the concentration much smaller than 1 M, and favorably compares with that of a typical LIB electrolyte, e.g., LiPF<sub>6</sub> in propylene carbonate. It gives ionic conductivities that are peaked at ~6 mS cm<sup>-1</sup> for concentrations around 1 M, but fall to the order of 1 mS cm<sup>-1</sup> or less for concentrations below 0.1 M.<sup>23</sup> The other lactone-based electrolyte, KF/GBL, achieved a fluoride concentration and ionic conductivity approximately half the corresponding values of CsF/GBL. The method did not apply to LiF and NaF, which are poorly soluble even in water. CsF is thus far superior to other salts as the primary source of fluoride ions in the present study. However, comparative use of KF as another option helps us not only support the proposed principle of the preparation method but also verify that both electrolytes offer electrochemically active fluoride ions independently of coexisting cations.

In a typical procedure GBL and 1.4 M CsF(KF) aqueous solution were mixed in a 10:1 volume ratio. The initial mixture formed an emulsion owing to the separation of the two phases at room temperature. Upon heating the mixture under continuous stirring, it soon de-emulsified before water began to vaporize at ~110 °C. We increased the temperature further to ~130 °C or above and continued heating for at least 40 min under Ar gas bubbling to reduce the residual water content to below 50 ppm. As discussed

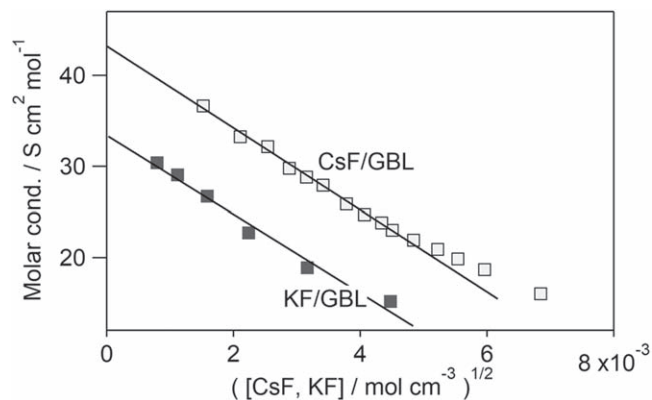


**Figure 1.** Molar ionic conductivities of a series of electrolytes diluted with neat GBL solvent from as-prepared CsF(KF)/GBL solution, as a function of the square root of CsF(KF) molar concentration after dilution.

below, during this process some of the initially water-solvated  $\text{Cs}^+(\text{K}^+)$  and  $\text{F}^-$  ions were subjected to gradual solvent substitution by GBL. An excess component eventually re-precipitated as solid CsF(KF). Additional precipitation occurred upon cooling the solution to room temperature, leaving a supernatant liquid that then served as the stable liquid fluoride electrolyte for the present study.

Figure 1 shows how the ionic conductivity changed by successive dilution of the as-prepared CsF(KF)/GBL with neat GBL solvent. In Fig. 1, the resultant molar ionic conductivity (in  $\text{S} \cdot \text{cm}^2 \cdot \text{mol}^{-1}$ ) is plotted as a function of the square root of the CsF(KF) molar concentration (in  $\text{mol} \cdot \text{cm}^{-3}$ ). The good linearity of both plots, except for the right-end portion, indicates that a sufficiently dilute series obeys Kohlrausch's law for strong electrolytes.<sup>12,13</sup> Furthermore, the limiting molar conductivity at infinite dilution, derived by the linear extrapolation in Fig. 1 ( $30\text{--}45 \text{ s} \cdot \text{cm}^2 \cdot \text{mol}^{-1}$ ) is comparable to those (in the range of  $34\text{--}45 \text{ s} \cdot \text{cm}^2 \cdot \text{mol}^{-1}$ ) reported for lithium salts dissolved in GBL.<sup>24,25</sup> These results suggest that CsF(KF) in GBL is most probably fully dissociated into individual  $\text{Cs}^+(\text{K}^+)$  and  $\text{F}^-$  ions.

We posit that the acidic  $\alpha$ -hydrogen next to the carbonyl group of GBL most likely plays a critical role in the interactions between the

GBL solvent molecules and  $\text{F}^-$  ions, as indirectly supported by DFT calculations (Fig. S2, Supplementary Material). At the high processing temperature used to prepare CsF(KF)/GBL, this interaction may even cause  $\alpha$ -hydrogen abstraction leading to the temporal formation of HF. The role of  $\alpha$ -hydrogen is further supported by the fact that  $\epsilon$ -caprolactone could be used as an alternative solvent; however, the present method invariably failed with other high-boiling solvents such as propylene carbonate, dimethyl sulfoxide, and *N*-methylpyrrolidone that lack analogous acidic hydrogen.

The possibility of HF formation during the preparation of CsF(KF)/GBL raises the question of whether fluoride ions therein could be present in the form of hydrogen difluoride ions,  $[\text{FHF}]^-$ . Even if CsF(KF)/GBL obeys Kohlrausch's law it might still contain species that form by undesirable reactions of GBL and could somehow be strongly bound to either  $\text{Cs}^+(\text{K}^+)$  or  $\text{F}^-$  ions as effective anion or cation acceptors. The residual water content might also have some relevance. A series of NMR spectra ( $^1\text{H}$ ,  $^{13}\text{C}$ ,  $^{19}\text{F}$ , and  $^{133}\text{Cs}$ ) were measured for CsF/GBL (Fig. 2) to provide insights into these fundamental questions.

First, the  $^{19}\text{F}$  spectrum in Fig. 2 had two main singlet peaks at  $\delta = -139.8$  and  $152.5$  ppm. Conversely  $[\text{FHF}]^-$ , in an electrolyte with a relatively low concentration of  $\sim 50$  mM, would have to be a doublet at  $\delta = -155.4$  ppm.<sup>26</sup> Furthermore,  $[\text{FHF}]^-$  is known to yield a  $^1\text{H}$  triplet at  $\delta = 16.6$  ppm.<sup>26</sup> No signals appeared at this position in the  $^1\text{H}$  spectrum in Fig. 2. Thus,  $[\text{FHF}]^-$  was not formed in CsF/GBL. Notably, any species other than the solvent molecules involved in the dissociation of CsF in GBL should be present at a concentration at least comparable to the resultant  $\text{Cs}^+$  and  $\text{F}^-$  ion concentrations. However, the baseline of the  $^{13}\text{C}$  spectrum in Fig. 2 had no features other than the solvent peaks. Although the  $^{13}\text{C}$  spectrum is much less sensitive than other forms of NMR spectra, these data exclude the possibility of additional hydrocarbon compounds at concentrations ( $>50$  mM) comparable with the  $\text{Cs}^+$  and  $\text{F}^-$  ions concentrations that give rise to distinct  $^{133}\text{Cs}$  and  $^{19}\text{F}$  signals in Fig. 2. The residual water content of less than 50 ppm ( $<3$  mM) cannot account for the dissociation of CsF to the concentration of 50 mM.

Thus, the fluoride ions in CsF(KF)/GBL are most likely in a simple form solvated by GBL. Several minor peaks visible in the  $^1\text{H}$  spectrum baselines in Fig. 2 might be related to this interaction; however, this point should be studied further in the future.

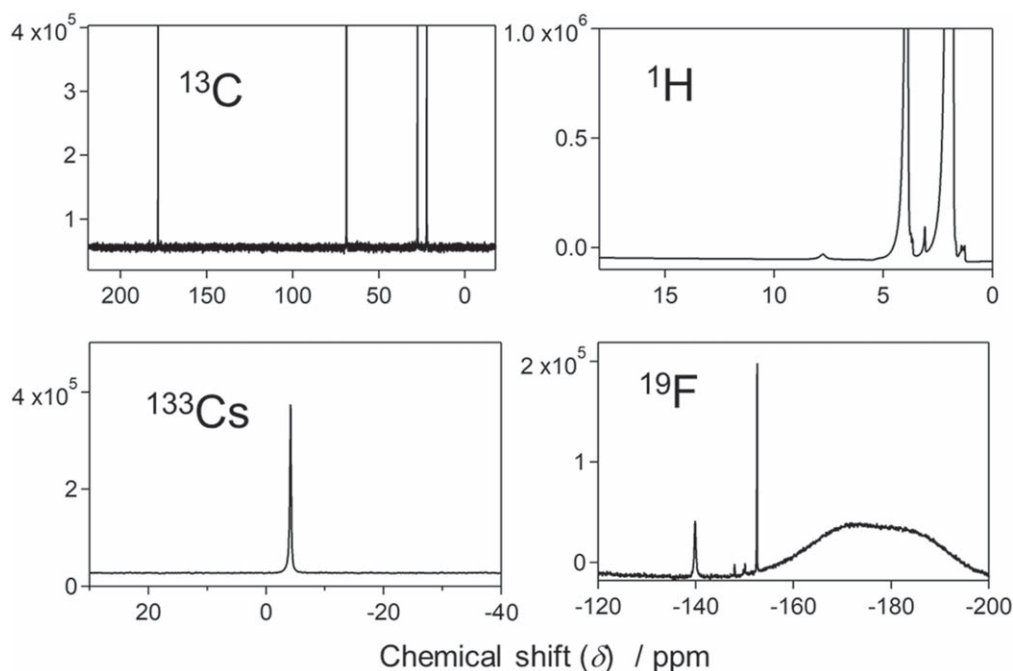


**Figure 2.** Series of NMR spectra measured for a representative CsF/GBL electrolyte fabricated in the present study.

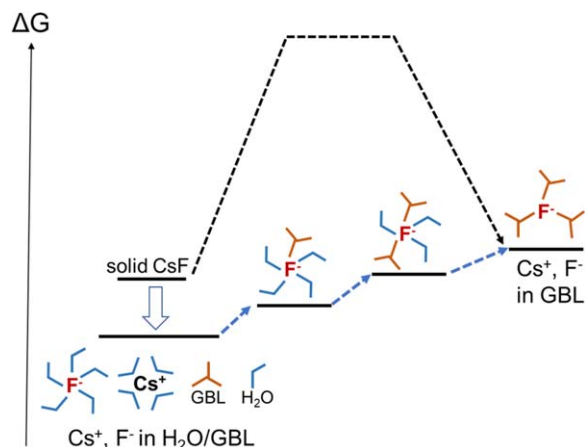


**Figure 3.** Schematic free energy diagram for a step-wise substitution of the solvation shell from water to GBL by a high temperature ( $\sim 130\text{ }^{\circ}\text{C}$ ) heat treatment of a mixture of GBL and aqueous CsF, allowing for a smooth “uphill” transformation to the final state. The direct path from solid CsF to CsF/GBL is kinetically disfavored. The initial, intermediate, and final solvation structures sketched by using symbolic  $\text{H}_2\text{O}$  and GBL molecules are only explanatory diagrams, not representing real molecular complexes.

**Thermodynamic and kinetic constraints on dissociation of CsF (KF) in GBL.**—GBL is a strongly polar organic solvent with a static dielectric constant of 39,<sup>27</sup> approximately half that of water. The fact that solid CsF(KF) is nevertheless normally insoluble in GBL should be interpreted with care. In practice, the maximum concentration of  $\sim 0.05\text{ M}$  for the  $\text{Cs}^+$  and  $\text{F}^-$  ions in CsF/GBL as achieved by the present method corresponds to the solubility product ( $K_{\text{sb}} = [\text{Cs}^+][\text{F}^-]$ ; unitless) of only  $2.5 \times 10^{-3}$  and, hence, to the positive standard Gibbs free energy of dissolution ( $\Delta G^0 = -RT \ln K_{\text{sb}}$ ) of  $14.6\text{ kJ}\cdot\text{mol}^{-1}$ . Here  $R$  and  $T$  are the gas constant ( $8.314\text{ J}\cdot\text{K}^{-1}\cdot\text{mol}^{-1}$ ) and the absolute temperature ( $293\text{ K}$  at room temperature), respectively. Thus, the state of CsF/GBL prepared by the present method is indeed thermodynamically disfavored compared with the crystalline state of CsF.

Nevertheless, the thermodynamic barrier of  $14.6\text{ kJ mol}^{-1}$  in terms of the standard Gibbs free energy of dissolution is not particularly high, and we suggest that it is more like a kinetic barrier that prevents the preparation of a similar CsF/GBL electrolyte by an ordinary procedure of mixing and stirring CsF powders in GBL. We observed that prolonged heating of a stirred mixture for many hours above  $130\text{ }^{\circ}\text{C}$  substantially increased the room-temperature ionic conductivity to several ten  $\text{mS}\cdot\text{cm}^{-1}$  without water, which supports the above thermodynamic considerations. The problem with this method is that the high-temperature heating of GBL in the presence of CsF powders caused the liquid to turn brown and the residual powders also changed color, likely because of some surface-catalyzed thermal reactions of GBL. The present method for fabrication of CsF(KF)/GBL allows us to circumvent such detrimental side reactions, and the process probably proceeds with an overall smaller kinetic barrier at the given temperature via step-wise solvent substitution (Fig. 3). Thus, a smooth “uphill” transformation to the novel liquid fluoride electrolyte is facilitated.

**Electrochemical activity of CsF(KF)/GBL.**—Plain metal electrodes requiring neither conductive supporting materials nor polymer binders are most effective for understanding the intrinsic capability of CsF(KF)/GBL to drive room-temperature metal/metal-fluoride transformation reactions. Figure 4a shows a collection of steady CVs recorded through 3–6 repeated cycles for a series of metal electrodes (Ag, Cu, Bi, Pb, and Zn; thin plate or foil) in CsF/GBL. The same CV series, but measured in an electrolyte without fluoride ions ( $0.5\text{ M LiFSA}$  solution in GBL), is shown on the right side (Fig. 4b).

In Fig. 4b, all the metal electrodes had a sharply rising (exceeding  $5\text{ mA}\cdot\text{cm}^{-2}$ ) anodic current that started at  $0.72$ ,  $0.26$ ,  $0.24$ ,  $-0.21$ , and  $-0.84\text{ V}$  vs the standard hydrogen electrode (SHE) for  $M = \text{Ag, Cu, Bi, Pb, and Zn}$ , respectively. These values roughly correlate with the standard-potential series,  $E^0(M/M^{x+})$ , for anodic metal dissolution. A relatively minor cathodic peak in the reverse scan represents a partial metal re-deposition. In contrast, the presence of  $\text{F}^-$  ions in CsF/GBL markedly affected the CV results (Fig. 4a). Broad peaks or plateaued anodic currents occurred, which we attribute to the formation of metal fluorides at the metal/electrolyte interface (as directly confirmed by XRD at a much higher level of charging; see below) followed by a reversible cathodic wave. Notably, Zn was the least noble metal that gave rise to such reversible CVs. This limitation is a major drawback of the present CsF(KF)/GBL electrolyte. Besides, the GBL solvent itself was not stable enough against oxidation in the far positive potential region beyond  $1.5\text{ V}$  vs SHE. This practically excluded positive electrode materials (such as Au) nobler than Ag.

The metal fluorination progresses to a certain depth of the metal bulk and effectively passivates the metal surface. If the resultant fluoride shell covers the entire surface and survives any subsequent reactions, it then naturally suppresses the anodic metal dissolution in CsF/GBL, as verified by a comparison of the results in Figs. 4a and 4b. The CV curves in CsF/GBL indicate how efficiently the fluoride shell grows during the anodic polarization, and how the shell undergoes reversible defluorination to restore the metallic phase during the cathodic reverse scan. From this viewpoint, Fig. 4a suggests that Cu underwent the least efficient fluorination because the corresponding CVs had an order of magnitude smaller current density than those of the other metals. This result can be attributed to the very low ionic (fluoride-ion) conductivity associated with the copper fluoride shell as discussed in more detail below. Note, that the actual ionic conductivity of metal fluorides is highly sensitive to the type and level of structural defects that accompany the state with which the fluoride participates in the redox reaction of interest. For example, a pure  $\text{BiF}_3$  crystal is a very poor ionic conductor with a room-temperature conductivity of the order of  $10^{-14}\text{ S cm}^{-1}$ .<sup>28</sup> If this low conductivity were also valid for the  $\text{BiF}_3$  shell formed in the present electrolyte, this would be at odds with the comparatively high fluorination efficiency of the Bi electrode in Fig. 4a and other relevant situations (see below).

To gain further kinetic insights into the reversible metal fluorination/de-fluorination processes in CsF(KF)/GBL, Fig. 5 compares CV results measured in CsF/GBL and KF/GBL for the Ag (Fig. 5a) and Cu (Fig. 5b) electrodes. The relatively large current densities associated with the Ag electrode suggest that the fluorination progressed deep into the metal bulk. We also confirmed in Fig. 5a that the higher fluoride concentration in CsF/GBL than in KF/GBL allowed for faster growth of the fluoride shell. The limited fluoride ion transport in the shell then naturally caused the anodic current to peak for further anodic polarization. In the case of KF/GBL (red curve in Fig. 5a); however, the anodic current tended to plateau rather than peak. This result can be attributed to the fluoride shell growing more slowly and the anodic scan reversing before the anodic peak sets in. The follow-up cathodic current for the reverse scan in Fig. 5 thus represents defluorination of the fluoride shell back to the metal phase. This invariably peaked as the fluoride shell decayed. For the Cu electrode, the low ionic conductivity of the fluoride shell is the main factor that determines the CV shape and the difference between CsF/GBL and KF/GBL becomes comparatively small (Fig. 5b).

**Charge-discharge behaviors of plain metal electrodes in CsF (KF)/GBL.**—*Cu electrode.*—Although the Cu electrode allowed for the least efficient fluorination, as noted above, the corresponding charge-discharge behaviors studied in constant current mode (Fig. 6) are worthy of attention first. Figure 6 shows the results of 25 cycles of charging and discharge. Except for some minor shifts between the respective curves, we observed essentially no capacity fading. The

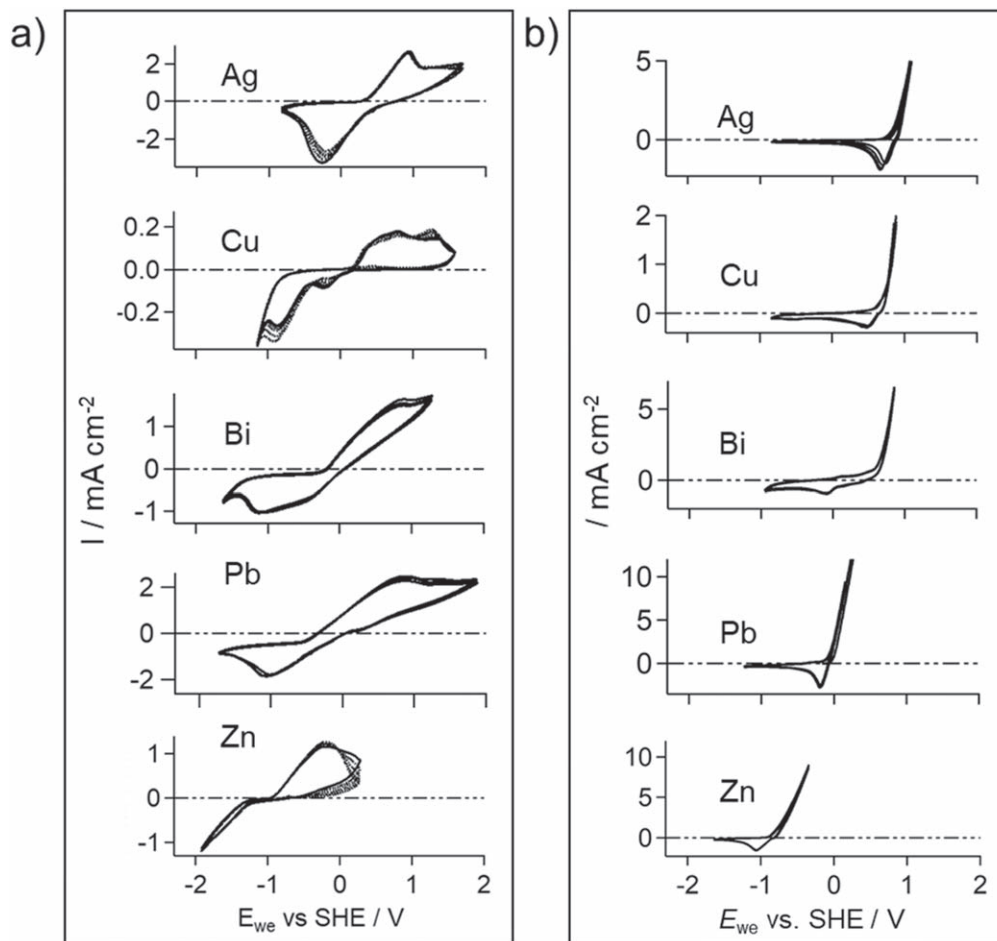


**Figure 4.** Series of steady CVs ( $10 \text{ mV s}^{-1}$ ) measured with various metals as the working electrodes in (a) CsF/GBL and (b) 0.5 M LiFSA/GBL containing no fluoride ions.

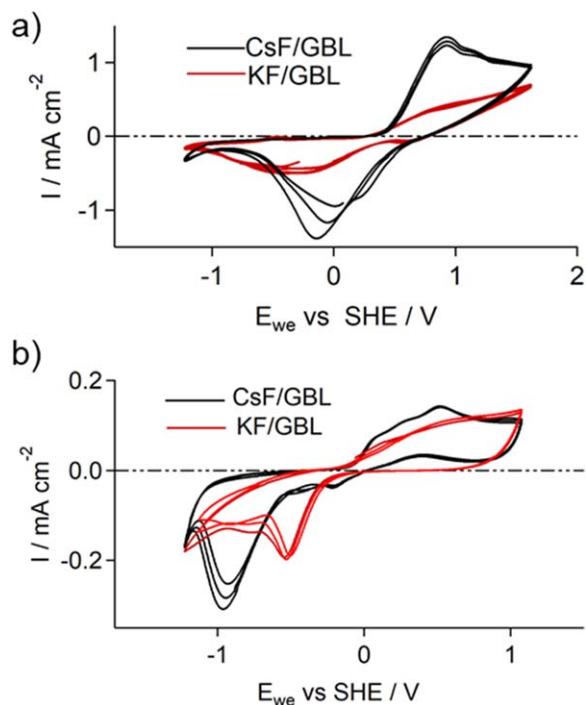


**Figure 5.** Comparison of CVs ( $10 \text{ mV s}^{-1}$ ) taken for (a) Ag and (b) Cu electrodes in CsF/GBL (black) and KF/GBL (red), respectively.

steeply rising anodic polarization on charging in the right end region for the small current density ( $i_c$ ) of  $0.031 \text{ mA.cm}^{-2}$  and the small capacity of only  $\sim 0.005 \text{ mAh.cm}^{-2}$  supports that limited fluorination of the Cu electrode restricted the resultant fluoride shell thickness. The corresponding reaction depth can be indirectly estimated from the theoretical capacity for Cu/CuF<sub>2</sub> of  $844 \text{ mAh.(g-Cu)}^{-1}$ , which is scaled with  $7560 \text{ mAh.cm}^{-2}$  for a Cu plate with a thickness of 1 cm. The experimental capacity of  $0.005 \text{ mAh cm}^{-2}$  then points to an effective reaction depth of only  $\sim 7 \text{ nm}$  ( $\sim 20 \text{ nm}$  in terms of the resultant fluoride shell thickness). This value, in turn, allows us to roughly estimate the effective fluoride ion conductivity ( $\sigma$ ) of the copper fluoride shell by assuming a polarization ( $V$ ) of 2 V across the shell with a thickness ( $d$ ) of  $\sim 20 \text{ nm}$  at an ionic-conductivity limited current density ( $i$ ) of  $0.03 \text{ mA.cm}^{-2}$ . The relationship,  $i = \sigma V/d$ , gives a quite small value of  $\sigma \approx 3 \times 10^{-11} \text{ S.cm}^{-1}$ .

It should be noted that direct experimental access to the actual ionic conductivities for the fluoride shells as formed on the metal surfaces in the present electrolyte is impractical irrespective of the shell thickness. Also, there are no literature values available for CuF<sub>2</sub>, probably because it is an even poorer ionic conductor than BiF<sub>3</sub> with a room-temperature ionic conductivity below  $\sim 10^{-14} \text{ S.cm}^{-1}$ . In any case, we presently have no choice but to make such an indirect estimate using the above-noted relationship. The estimated value is small but still orders of magnitude larger than  $10^{-14} \text{ S.cm}^{-1}$ . This implies that the copper fluoride shell with a nanometer-scale thickness may be highly defective.

**Pb electrode.**—The Pb electrode is at the other extreme, with a reported ionic conductivity of  $\beta\text{-PbF}_2$  at room temperature of the

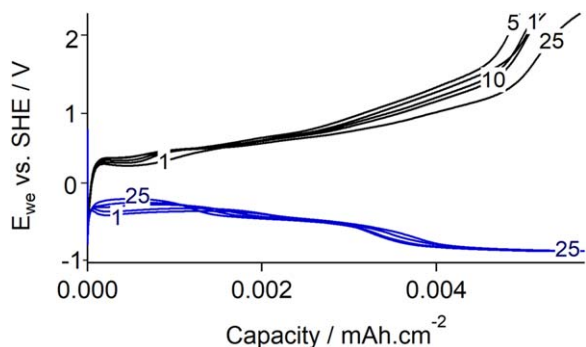


**Figure 6.** Charge (black) and discharge (blue) curves at a current density of  $0.031 \text{ mA cm}^{-2}$ , for a total of 25 cycles of a Cu electrode in CsF/GBL. Numbers ( $n$ ) attached to the curves show the  $n$ th cycle.

order of  $10^{-8}$  to  $10^{-7} \text{ S cm}^{-1}$ .<sup>29</sup> As shown in Fig. 7a, the Pb electrode allowed for smooth charging and capacities exceeding  $0.1 \text{ mAh.cm}^{-2}$  with a minor polarization ( $\sim 0.1 \text{ V}$ ) at a comparatively high current density of  $0.25 \text{ mA.cm}^{-2}$ . This capacity was more than enough for us to verify the formation of an orthorhombic phase of  $\text{PbF}_2$ <sup>30</sup> by XRD analysis, as shown by profile *b* in Fig. 7b. The  $\text{PbF}_2$  signals almost disappeared by discharge (profile *c*) to further support the reversible charge and discharge behavior. Here, care should be taken because the diffraction peaks due to the bulk metal plate located underneath are always overwhelmingly stronger

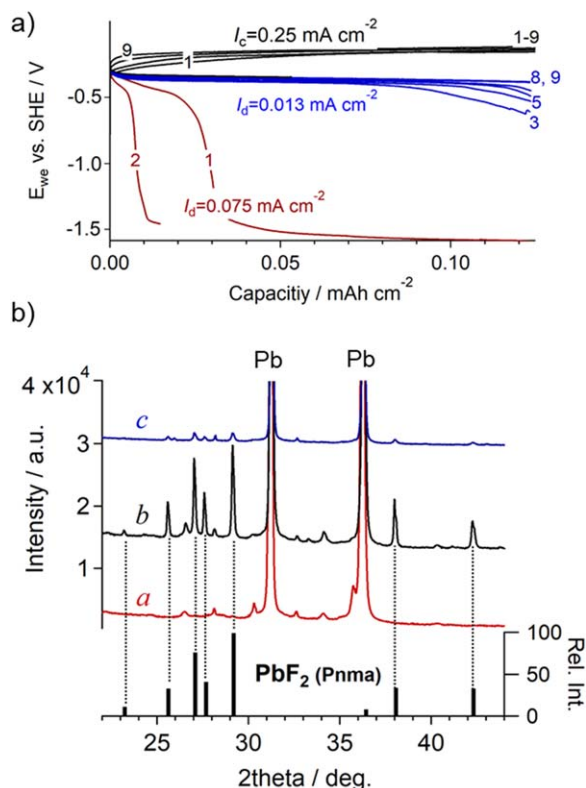


**Figure 7.** (a) Charge and discharge curves for a total of 9 cycles for a Pb electrode in CsF/GBL. The current density for charging was fixed at  $0.25 \text{ mA cm}^{-2}$ , whereas that for the discharge was switched from  $0.075$  to  $0.013 \text{ mA cm}^{-2}$  for the 3rd and subsequent cycles. (b) An offset series of ex-situ XRD patterns measured for a pristine Pb plate (*a*, red), after a one-time charge for  $0.15 \text{ mAh cm}^{-2}$  (*b*, black), and after subsequent discharge (*c*, blue). Observed peaks in pattern *b* coincide with the standard powder XRD pattern for the orthorhombic phase (Pnma) of  $\text{PbF}_2$ , shown at the bottom. Note that the diffraction peaks labeled Pb, associated with the bulk metal plate underneath, are two orders of magnitude stronger in intensity than the fluoride signals, with the peak tops far outside of the vertical axis range.

than the signals associated with the fluoride shell. In this situation, what XRD can provide as evidence for the reversible metal/metal-fluoride transformation are only such fluoride signals that grow by charging and decay by discharge.

In Fig. 7a, we cut off the constant-current charging at a capacity of  $\sim 0.1 \text{ mAh.cm}^{-2}$  despite that the charging curve manifested still only minor polarization or the charging did not yet reach the ionic-conductivity-limited stage. However, based on the theoretical capacity for  $\text{Pb/PbF}_2$  of  $2934 \text{ mAh.cm}^{-2}$ , the capacity of  $0.1 \text{ mAh.cm}^{-2}$  already gives the average  $\text{PbF}_2$  thickness of  $\sim 500 \text{ nm}$ , which is sufficient to yield distinguishable XRD signals (Fig. 7b). Furthermore, a series of FE-SEM and EDX imaging (Fig. 8) at this limited capacity illuminates a significant correlation between the charge-discharge curves and the morphologies of the  $\text{PbF}_2$  shells. Figure 8b demonstrates that the fluorinated (charged) state of the Pb plate in the first cycle already developed a considerably rugged and granular surface morphology associated with the  $\text{PbF}_2$  shell, whereas the subsequent discharge (Fig. 8c) restored a planar morphology similar to that of the pristine state (Fig. 8a). The EDX mapping (Fig. 8d) for the charged state indicates that the F signal aroused predominantly from discrete grains constituting the fluoride shell, while the signals in the blurred Pb map from both the fluoride and the underlying metal plate. We also observed reversible changes between these morphologies for up to nine cycles (Fig. S3), which parallels with the well-reversible charge-discharge curves at a low discharge rate (Fig. 7a).

The metal fluorination causes a substantial increase in the specific molar volume and, hence, in the local stress at the metal/metal-fluoride interfacial region, so that it never proceeds in a layer-by-layer fashion nor gives a uniform thickness of the fluoride shell. The granular morphology with individual grains having dimensions of hundreds of nm or more also points to a considerable reconstruction of the  $\text{PbF}_2$  shell. In the relatively early stages of charging, this allows for minor coverage of the fluoride shell in significant parts of the Pb electrode. This, in turn, explains the minor polarization accompanying the charging curves in Fig. 7a. We separately confirmed that the ionic-conductivity-limited charging with steadily increasing polarization started at a capacity exceeding  $0.3 \text{ mAh.cm}^{-2}$  corresponding to the average  $\text{PbF}_2$  shell thickness of  $1.5 \mu\text{m}$  (Fig. S4). In this regime, the granular morphology turned to a more continuous and complete one that covered the whole surface (Fig. S5). The indirect way to estimate the ionic conductivity for the  $\text{PbF}_2$  shell in this regime leads to a value of the order of  $10^{-7} \text{ S.cm}^{-1}$ , which is comparable to the literature values quoted above for the highly conducting  $\beta$  phase of  $\text{PbF}_2$ .

Notably, Fig. 7a also reveals a strongly asymmetric current-density dependence between charging and discharge. Unless we used an order of magnitude lower discharge current than that used for charging, rapid capacity fading was unavoidable. This behavior likely results from the fluorination/defluorination dynamics involving the metal electrode, as schematically illustrated in Fig. 9. Note that Fig. 9 should be interpreted as modeling a local cross-section of a metal/metal-fluoride interfacial region regardless of the actual morphologies. In the anodic process (Fig. 9a), oxidation (de-electronation) occurs from the metal side (Fermi level) of the metal/fluoride interface, followed by binding of mobile fluoride ions to the resultant metal cations leading to net growth of the fluoride shell. This process does not require a large polarization (for electronic activation) and proceeds rather efficiently if only a high enough fluoride ion conductivity is assured in the fluoride shell. Note that this anodic reaction also requires the fluoride ion transfer from the electrolyte for completion, which must involve desolvation. However, it probably occurs with also a minor activation judging from the overall smooth progression of the reaction at relatively high charging rates and with minor polarization.

By contrast, the reverse process (Fig. 9b) involves reduction (electronation) of the “electronically insulating” fluoride shell. We, therefore, expect a considerable electronic energy barrier to accompany this step unless the fluoride shell is rich in some defect-induced

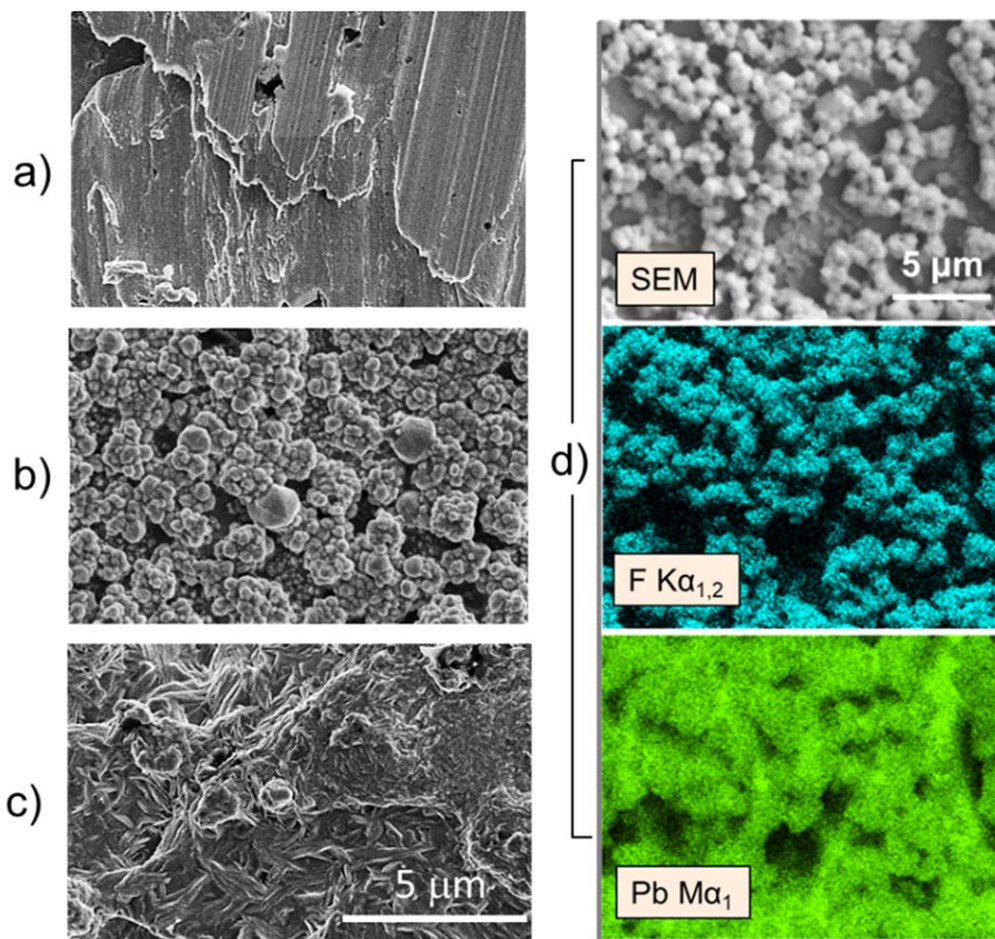


**Figure 8.** Typical FE-SEM images (on the left) taken for (a) pristine, (b) one-time charged to  $0.13 \text{ mAh cm}^{-2}$ , and (c) fully discharged states of the Pb electrode. (d) EDX mapping images for F (center) and Pb (bottom) corresponding to the SEM image shown atop, as obtained for a relatively low-capacity charged state with a granular  $\text{PbF}_2$  morphology.

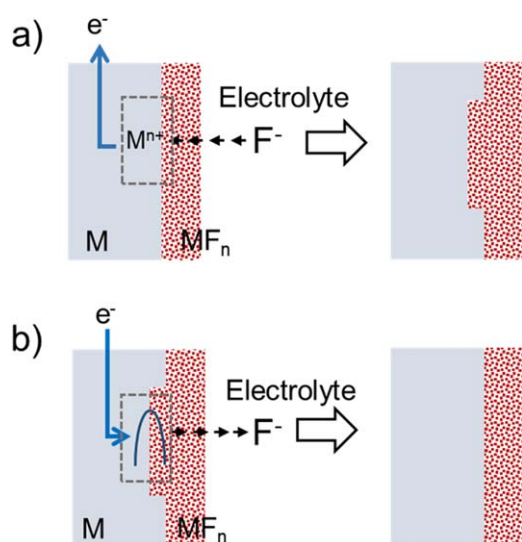


**Figure 9.** Schematic illustration of (a) the anodic fluorination of a metal electrode and (b) defluorination to reform the metal phase from the fluoride shell, accompanied by a significant energy barrier associated with the metal-to-insulator electron transfer. The fluoride shell must have a high enough fluoride-ion conductivity to ensure fluoride-ion transport across the shell in both anodic and cathodic processes.

electron-accepting levels. This situation accounts for the need for a sufficiently low discharge rate to avoid the rapid capacity fading. The excess negative charge associated with the injected electrons, which are taken up for the reduction of  $\text{MF}_n$ , must then be compensated by fluoride ion transport from the metal/metal-fluoride interface to the electrolyte at a distance. A large enough fluoride ion conductivity is thus imperative for this cathodic reaction as well.

*Other metal electrodes.*—We confirmed reversible fluorination also for Ag, Bi, and Zn electrodes on a half-cell basis from their charge-discharge curves and noticeable XRD signals associated with the respective fluoride species formed in the charged states (Figs. S6, S8, and S10). We have also observed characteristic morphologies of the respective fluoride shells by FE-SEM in combination with EDX elemental mapping (Figs. S7, S9, S11), although the fluorinated Ag and Zn surfaces remain to be studied further because the silver fluoride shell was damaged easily by the electron beam and strong EDX signals from Cs mixed in the case of zinc fluoride shell (Fig. S11).

Here, we restrict to the model full-cell operation of  $\text{ZnF}_2/\text{Zn}||\text{F}^-||\text{AgF}/\text{Ag}$ . Both Zn and Ag are not necessarily promising materials for future application to FSBs, but in the present study they provide the only combination with which we can demonstrate the feasibility of a cell working with an output voltage greater than 1 V. The Ag electrode was sized order of magnitude smaller than the pre-fluorinated Zn electrode as a counter electrode. The pre-fluorination of Zn was achieved by charging it in advance in a separate cell in the half-cell mode to capacity with which the



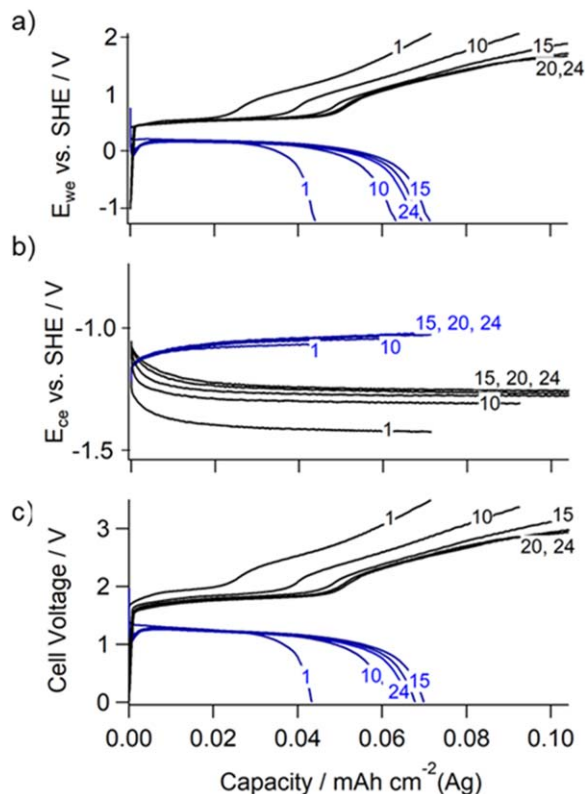


**Figure 10.** Charge and discharge curves for a total of 24 cycles for an Ag-Zn formal full cell in CsF/GBL. The Ag plate electrode had dimensions of 4 mm<sup>2</sup>, roughly an order of magnitude smaller than that of the pre-fluorinated Zn plate electrode (~25 mm<sup>2</sup>). Both charge and discharge currents were set to be 25  $\mu$ A. (a), (b) Charge-discharge curves of the Ag and Zn electrodes, respectively. (c) Charge-discharge profiles of the full-cell voltage.

full-cell charge and discharge performance is controlled exclusively by the capacity of the Ag electrode. In Fig. 10, the potentials of the individual electrodes and the difference between them (i.e., the full-cell voltage) are plotted as functions of this positive-electrode-limited capacity per unit area of the Ag electrode.

As shown in Fig. 10a, the Ag electrode exhibited charge-discharge cycle behavior with well-defined charge and discharge plateaus but was accompanied by a noticeably large irreversible capacity. Besides both charge and discharge capacities showed an increasing trend by cycling. Analogous behaviors occurred also at the time of Ag half-cell operation (Fig. S8). Although the potential window of CsF(KF)/GBL extends to above 1.5 V vs SHE (Figs. 4 and 5), the advanced stage of charging of Ag under increased polarization might still suffer from irreversible solvent reactions. A potential vulnerability of AgF as the charging product, due e.g., to partial dissolution to the electrolyte, can also cause the problem as it prevents AgF from contributing fully to discharge. Whatever changes by cycling that mitigate these effects lead to improved capacities by cycling, but further study is necessary for better clarification of this issue.

In Fig. 10b, the potential of the Zn electrode with a large excess area switched between the two extended discharge and charge plateaus, as expected. The overall cell voltage curves (Fig. 10c) thus closely resembled the shapes of the charge-discharge curves (Fig. 10a) of the Ag electrode. The observed maximum cell voltage at the discharge plateau, ~1.3 V, compares with the difference (1.76 V) between the standard redox potentials of Ag/AgF and Zn/ZnF<sub>2</sub>, as calculated from the standard Gibbs free energies of formation of AgF (-187 kJ mol<sup>-1</sup>) and ZnF<sub>2</sub> (-713.3 kJ mol<sup>-1</sup>), by taking an overall discharge polarization of ~0.4 V into account.

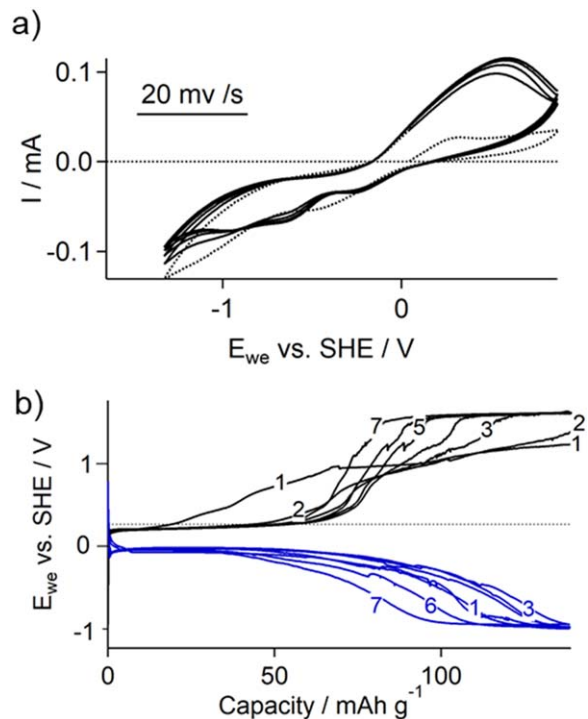


**Figure 11.** (a) Reversible CV curves measured for a Bi composite electrode in KF/GBL. The thin dotted curve corresponds to the first cycle starting with anodic polarization. (b) Charge (at ~0.2 C; black) and discharge (at ~0.04 C; blue) curves for 7 cycles (12 h per cycle) obtained after the CV measurements.

#### Charge-discharge characteristics of composite electrodes.—

Composite electrodes, consisting of mixed particulates of active materials of interest and conductive additives (e.g., carbon) dispersed in a polymer binder matrix, are extremely complex compared with the plain metal electrodes used in the aforementioned model experiments. The individual particles of active materials do not necessarily have equivalent access to the electrolyte, such that preceding charge or discharge reactions may either positively or negatively affect the reactions of nearby particles. The simple mechanism for the plain metal electrodes, as depicted in Fig. 9, is no longer valid under such circumstances. Furthermore, the electron conduction pathways afforded by the intricate carbon network are vulnerable, and substantial volume changes of the active material are associated with the charge and discharge reactions. The control of reversible fluorination/defluorination processes with these considerations is challenging in many respects.

To date, electrochemical behaviors of composite electrodes in CsF(KF)/GBL have only been studied in some detail (including convincing XRD data) for systems composed of Bi particles. We there found that CsF/GBL electrolyte in combination with composite Bi electrodes caused unexpected non-redox reactions with fluorinated Bi particles to form mixed fluorides such as CsBiF<sub>6</sub><sup>31</sup> and CsBi<sub>2</sub>F<sub>7</sub>.<sup>32</sup> Therefore, in the following experiments we used KF/GBL to avoid this additional complexity. Figure 11 shows an example of the results obtained for a composite made of Bi micro powders (-100 mesh; < 150  $\mu$ m), acetylene black, and PVDF mixed in an 88:8:8 weight ratio. The composite was loaded on an Al current collector foil for a total weight per unit area of ~4 mg cm<sup>-2</sup>. Figure 11a shows the reversible CV curves obtained for the composite electrode. Unlike the neat metal electrode polished immediately before use, the Bi composite had a native surface oxide layer, which interfered with fluorination of the Bi particles in the initial CV scan from the anodic direction (the dotted curve).

Figure 11b shows a collection of the charge and discharge curves measured for 7 cycles, where we used a moderately high rate of

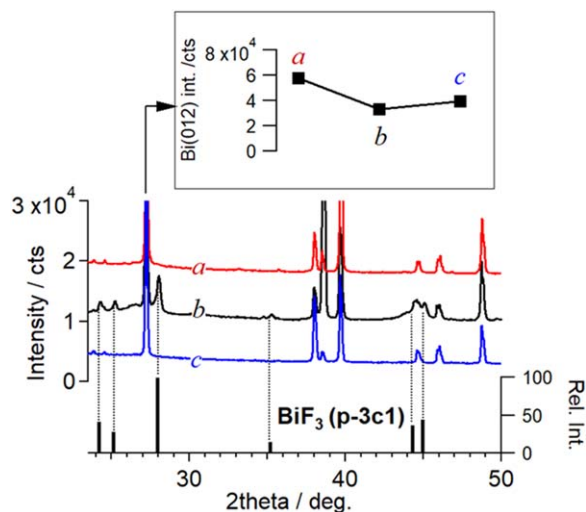


**Figure 12.** Comparison of ex-situ XRD patterns measured for a pristine Bi composite electrode (pattern *a*, red), after a one-time charge for  $\sim 120 \text{ mAh g}^{-1}$  (pattern *b*, black), and after full discharge (pattern *c*, blue) corresponding to the 7th cycle curve in Fig. 11b. The inset graph in the upper frame shows how the intensity of the major Bi-metal peak for the 012 Bragg reflection changed accordingly. The bar graph below shows the standard powder XRD pattern of trigonal  $\text{BiF}_3$ , matching a series of new peaks that appeared in the charged state.

$\sim 0.2 \text{ C}$  [ $75 \text{ mA} \cdot (\text{g-Bi})^{-1}$ ] for charging, and a low rate of  $\sim 0.04 \text{ C}$  [ $15 \text{ mA} \cdot (\text{g-Bi})^{-1}$ ] was needed for discharge to observe a distinguishable discharge plateau with minor polarization. Under these operating conditions, we obtained a capacity roughly one-third of the theoretical capacity for Bi ( $380 \text{ mAh g}^{-1}$ ), although a capacity-fading trend became obvious at 3–5 cycles. An irregular behavior of the first charge curve and the opposite tendency for the capacity to increase over the initial cycling may be explained as follows. First, the composite electrode consists of significantly large Bi particles (in tens of micrometers regime) probably not allowing so efficient fluorination. The presence of native oxide layers also disturbs the charging, thus increasing the polarization earlier than usual. The subsequent low-lying extended plateau possibly reflects the anodic dissolution of Bi particles inadequately passivated by the fluoride shell. Note that the dissolved  $\text{Bi}^{3+}$  cations, together with the nearby fluoride ions, can in part also give rise to fine deposits of bismuth fluorides. The subsequent defluorination by discharge will then lead to fine, even nanoscale, Bi particles that facilitate the fluorination in the next step of charging. The well-fluorinated Bi particles also mitigate anodic dissolution and shift the high-polarization plateau to a significantly more positive potential. Overall, the capacity tends to increase by cycling first but eventually subjected to fading due to some other competing irreversible processes.

Figure 12 compares the XRD patterns obtained for the Bi composite electrode in its pristine state, after one-time charging to  $\sim 120 \text{ mAh/g-Bi}$ , and a fully discharged state corresponding to that of the 7th (last) cycle in Fig. 11b. The new peak appearing in the charged state (pattern *b*) is assigned to the trigonal (p-3c1) phase of  $\text{BiF}_3$ . In the fully discharged state (pattern *c*), fluoride peaks were no longer visible. The inserted plot in the upper frame shows that the major Bi-metal peak attributed to the 012 Bragg reflection decreased by  $\sim 40\%$  the value of the first charge. This result agrees with the experimental capacity of one-third of the theoretical capacity. Overall, these results (Figs. 11 and 12) confirm the occurrence of reversible fluorination in the Bi composite electrode in KF/GBL.

**Upgrading CsF(KF)/GBL for higher performance.**—The experimental results presented and discussed above confirm the fundamental capabilities of CsF(KF)/GBL, as a novel non-aqueous liquid fluoride electrolyte that enables reversible electrochemical

fluorination/defluorination of various metal electrodes at room temperature. However, there remains a major issue that prevents the electrolytes from being applied to practical FSBs with high ( $> 2 \text{ V}$ ) cell voltages. This is because CsF(KF)/GBL undergoes an irreversible reductive sub-reaction of the solvent in the negative potential region beyond ca.  $-1.5 \text{ V}$  vs SHE. This strongly limits the choice of active materials and excludes many useful candidate negative electrode materials that are less noble than Zn. The trace amount of residual water is not involved in this reaction causing a continuous large irreversible cathodic current once the potential reaches this region. The onset potential of this sub-reaction is too positive to be related to the intrinsic reductive decomposition of GBL. The virtually free fluoride ions interacting with only the solvent molecules in the electrolyte might have a critical role in facilitating this undesirable electrochemical reaction. Thus, there is a need to further adjust or optimize the chemical activity of fluoride ions in CsF(KF)/GBL for them to work solely as fluorination agents that selectively react with metals.

## Conclusions

For the development of fluoride shuttle batteries (FSBs) operating at room temperature, there is a need to develop a liquid electrolyte that offers fluoride ions that have not only sufficient conductivity in the liquid but also strong reactivity with various metals to form their fluoride salts. Whether or not these fundamental criteria are met depends on the state of fluoride ions in the electrolyte in terms of their solvation structure and interactions with other coexistent molecular or ionic species. We have established a method to fabricate lactone-based liquid electrolytes, CsF(KF)/GBL, composed of either CsF or KF. The fluoride salts dissociate in GBL to a maximum concentration of  $\sim 50 \text{ mM}$  affording an ionic conductivity exceeding  $0.5 \text{ mS cm}^{-1}$ . This strong electrolyte can drive reversible fluorination at room temperature for a wide range of metals from Ag to Zn.

In every case of a plain metal electrode studied on a half-cell or model full-cell basis, we verified superior charge-discharge cyclability compared with those previously reported based on more complex liquid electrolytes. We also confirmed the formation of metal fluorides by charging and reversible defluorination back to the metal by discharge based on *ex-situ* XRD analyses. Therefore, the fluorination reaction progresses to a depth of hundreds of nm into the metal bulk, for most electrode metals other than Cu, which had a very low fluorination capacity. Reversible half-cell operation was also verified for a conventional carbon-polymer composite electrode consisting of Bi particles.

A practical problem with the CsF(KF)/GBL electrolytes in their present form is their limited negative potential window, which currently excludes active materials less noble than Zn for the negative electrode. This result is most likely attributed to the presence of fluoride ions that assist in promoting irreversible electrochemical decomposition of the solvent at the negative electrode.

## Acknowledgments

This work is based on results obtained from a project, “Research and Development Initiative for Scientific Innovation of New Generation Batteries (RISING2),” JPNP16001, commissioned by the New Energy and Industrial Technology Development Organization (NEDO). We thank Andrew Jackson, PhD, from Edanz Group (<https://en-author-services.edanzgroup.com/ac>) for editing a draft of this manuscript.

## ORCID

Mitsuo Kawasaki <https://orcid.org/0000-0002-4642-5755>

## References

- M. A. Reddy and M. Fichtner, *J. Mater. Chem.*, **21**, 17059 (2011).
- F. Gschwind, G. Rodriguez-Garcia, D. J. S. Sandbeck, A. Gross, M. Weil, M. Fichtner, and N. Hörmann, *J. Fluorine Chem.*, **182**, 76 (2016).
- N. Nitta, F. Wu, J. T. Lee, and G. Yushin, *Mater. Today*, **18**, 252 (2015).

4. A. M. Haregewoin, A. S. Wotango, and B.-J. Hwang, *Energy Environ. Sci.*, **9**, 1955 (2016).
5. M. A. Hannan, M. D. M. Hoque, A. Hussain, Y. Yusof, and P. J. Ker, *IEEE Access*, **6**, 19362 (2018).
6. I. Mohammad, R. Witter, M. Fichtner, and M. A. Reddy, *ACS Appl. Energy Mater.*, **1**, 4766 (2018).
7. K. Okazaki, Y. Uchimoto, T. Abe, and Z. Ogumi, *ACS Energy Lett.*, **2**, 1460 (2017).
8. V. K. Davis et al., *Science*, **362**, 1144 (2018).
9. H. Konishi, T. Minato, T. Abe, and Z. Ogumi, *Chem. Lett.*, **47**, 1346 (2018).
10. H. Konishi, T. Minato, T. Abe, and Z. Ogumi, *J. Appl. Electrochem.*, **48**, 1205 (2018).
11. H. Konishi, T. Minato, T. Abe, and Z. Ogumi, *J. Electroanal. Chem.*, **826**, 60 (2018).
12. R. M. Fuoss, *J. Solution Chem.*, **7**, 771 (1978).
13. M. Çetin, *Phys. Rev. E*, **55**, 2814 (1997).
14. J. W. Emsley and L. Phillips, *Prog. Nucl. Magn. Reson. Spectrosc.*, **7**, 1 (1971).
15. N. Mozhzhukhina and E. J. Calvo, *J. Electrochem. Soc.*, **164**, A2295 (2017).
16. Y. Li, K. Leung, and Y. Qi, *Acc. Chem. Res.*, **49**, 2363 (2016).
17. T. Minato and T. Abe, *Prog. Surf. Sci.*, **92**, 240 (2017).
18. H. Konishi, T. Minato, T. Abe, and Z. Ogumi, *J. Electrochem. Soc.*, **164**, A3702 (2017).
19. H. Konishi, T. Minato, T. Abe, and Z. Ogumi, *Mater. Chem. Phys.*, **226**, 1 (2019).
20. A. C. Kucuk, T. Minato, T. Yamanaka, and T. Abe, *J. Mater. Chem. A*, **7**, 8559 (2019).
21. B. Delley, *J. Chem. Phys.*, **92**, 508 (1990).
22. B. Delley, *J. Chem. Phys.*, **113**, 7756 (2000).
23. K. Kondo, M. Sano, A. Hiwara, T. Omi, M. Fujita, A. Kuwae, M. Iida, K. Mogi, and H. Yokoyama, *J. Phys. Chem. B*, **104**, 5040 (2000).
24. M. Ue, *J. Electrochem. Soc.*, **141**, 3336 (1994).
25. X. He, W. Pu, J. Han, J. Chen, J. Lu, C. Jiang, and C. Wan, *J. Phys. Chem. B*, **109**, 23141 (2005).
26. I. G. Shenderovich, S. N. Smirnov, G. S. Denisov, V. A. Gindin, N. S. Golubev, A. Dunger, R. Reibke, S. Kirpekar, O. L. Malkina, and H.-H. Limbach, *Ber. Bunsenges. Phys. Chem.*, **102**, 422 (1998).
27. D. R. Lide (ed.), *CRC Handbook of Chemistry and Physics* (CRC Press, Boca Raton, FL) 75th ed., p. 160 (1994).
28. M. W. Shafer, G. V. Chandrashekar, and R. A. Figat, *Solid State Ionics*, **5**, 633 (1981).
29. R. W. Bonne and J. Schoonman, *J. Electrochem. Soc.*, **124**, 28 (1977).
30. Y. Xu, M. Yamazaki, and P. Villars, *Jpn. J. Appl. Phys.*, **50**, 11RH02 (2011).
31. K. O. Christe, W. W. Wilson, and C. J. Schack, *J. Fluorine Chem.*, **11**, 71 (1978).
32. A. A. Kaminskii, A. V. Butashin, and S. N. Sul'yanov, *Inorg. Mater.*, **32**, 98 (1996).